Accepted Manuscript

Application of 3D heat diffusion to detect embedded 3D empty cracks

C. Serra, A. Tadeu, J. Prata, N. Simões

Please cite this article as: C. Serra, A. Tadeu, J. Prata, N. Simões, Application of 3D heat diffusion to detect embedded 3D empty cracks, *Applied Thermal Engineering* (2013), doi: 10.1016/j.applthermaleng.2013.08.037.

Application of 3D heat diffusion to detect embedded 3D empty cracks

C. Serra[a,*], A. Tadeu[b], J. Prata[c], N. Simões[d]

[a]ITeCons - Instituto de Investigação e Desenvolvimento Tecnológico em Ciências da Construção, Rua Pedro Hispano s/ n., 3030-289 Coimbra, Portugal
e-mail: cserra@itecons.uc.pt
*Corresponding author

[b]Department of Civil Engineering, University of Coimbra, Pólo II, Rua Luís Reis Santos, 3030-788 Coimbra, Portugal
e-mail: tadeu@dec.uc.pt

[c]Department of Civil Engineering, University of Coimbra, Pólo II, Rua Luís Reis Santos, 3030-788 Coimbra, Portugal
e-mail: jprata@itecons.uc.pt

[d]Department of Civil Engineering, University of Coimbra, Pólo II, Rua Luís Reis Santos, 3030-788 Coimbra, Portugal
e-mail: nasimoes@dec.uc.pt

List of Acronyms

3D - Three-dimensional
BEM - Boundary element method
IRT - Infrared thermography
NDT - Non-destructive testing technique
REC - Receiver placed in a specific location on the grid of receivers G1
REF - Case of an infinite sized crack with null heat fluxes
TBEM - Normal-derivative integral equations formulation of the boundary element method

Abstract

This paper presents a 3D boundary element model (BEM), formulated in the frequency domain, to simulate heat diffusion by conduction in the vicinity of 3D cracks. The model intends to contribute to the interpretation of infrared thermography (IRT) data results and to explore the features of this non-destructive testing technique (NDT) when it is used to detect and characterize defects. The defect is assumed to be a null thickness crack embedded in an unbounded medium. The crack does not allow diffusion of energy, therefore null heat fluxes are prescribed along its boundary. The BEM is written in terms of normal-derivative integral equations (TBEM) in order to handle null thickness defects. The resulting hypersingular integrals are solved analytically.

The applicability of the proposed methodology to defect detection tests is studied once the TBEM results have been verified by means of known analytical solutions. Heat diffusion generated by a 3D point heat source placed in the vicinity of a crack is modeled. The resulting thermal waves phase is compared with that obtained when the defect is absent, so as to understand the influence of crack characteristics on the IRT data results analysis, especially on the phase-contrast images. Parameters such as the size of the crack, its shape, its position (buried depth and inclination) and its distance from the heat source are analyzed. Some conclusions are drawn on the effects of varying those parameters.

Keywords: 3D heat sources, infrared thermography, normal-derivative integral equations (TBEM), transient heat diffusion, phase-contrast.

1. Introduction

Heat and moisture diffusion is sensitive to the presence of defects. The analysis of thermal pattern images collected via infrared thermography (IRT) has therefore proven to be a useful non-destructive technique (NDT) for defect detection in a wide range of applications and sectors. An NDT involving IRT can be performed by taking a passive approach if the materials and structures are tested in their natural state. If relevant thermographic data are not obtained an active approach can be taken, in which an additional heat source is used to generate the temperature difference which is not produced otherwise [1]. Thermal imaging is generally used in building diagnostics for detecting heat loss, missing or damaged insulation, thermal bridges, air leakages and excess moisture [2]. However, since the properties of subsurface defects can be detected and their quantitative characterization achieved by solving heat transfer problems using active IRT data, active IRT has been extensively used in NDT tests in a wide range of applications, including civil engineering ([3],[4]).

Different types of active IRT can be used, depending on how the surfaces are stimulated to produce a temperature gradient in the test specimen [5]. One type is lock-in thermography, where both thermal and phase images' results are recorded. Phase images are less influenced by surface characteristics and less sensitive to non-uniform heating and do not require the previous knowledge of the position of non-defect areas that is required in simple thermal contrast processing.

According to Maldague [5] comparisons between numerical models and experimental results are not straightforward, but such modeling gives useful information about the general thermal behavior of the sample, and it is useful to establish the limits of the effectiveness of IRT and set inspection parameters. Furthermore, it allows the consideration of different defect geometries, to determine their detectability and the expected optimum observation time window for the best subsurface defect visibility without the expense of making and testing specimens. This attests to the interest in solving heat transfer problems for the detection and quantitative characterization of the properties of subsurface defects. However, the 3D nature of subsurface defects combined with the need to simulate heat transfer and diffusion phenomena in a transient regime presents a challenge for researchers ([6],[7]).

Of the available numerical methods for homogeneous unbounded or semi-infinite systems modeling, the BEM is the one that automatically satisfies far field conditions and therefore only requires the discretization of the inclusion's boundaries [8]. Unlike domain-discretization based techniques which

give sparse systems of equations, the BEM allows a compact description of the regions, resulting in fully populated systems of equations. The major drawbacks of the BEM are that it requires the prior knowledge of the fundamental solution, and that it may lead to singular or nearly singular integrals. However, it is still considered to be one of the best tools for this kind of problem.

When the thickness of the heterogeneity being modeled tends towards zero, as in the case of cracks or thin defects, the conventional direct BEM degenerates and becomes inaccurate. Various techniques have been proposed to overcome this, such as the normal-derivative integral equations formulation (TBEM), which leads to hypersingular integrals. Various numerical methods have been proposed to overcome difficulties posed by such singularities ([9],[10],[11],[12],[13]).

This paper describes a model motivated by an interest in assessing the potential of using IRT in the presence of defects with specific geometries and depths. In the sections that follow, the problem is first defined and the TBEM formulated in the frequency domain is presented. Analytical solutions are used to solve the hypersingular integrals that appear in the 3D TBEM formulation, when the element being integrated is the loaded one. Finally, we describe the methodology used to obtain time-domain responses from frequency-domain calculations, followed by a number of numerical applications to illustrate the applicability and usefulness of the proposed approach in the analysis of several test cases, with the simulation of heat diffusion generated by a point heat source placed in the vicinity of a crack. These applications focus mainly on the effects on the resulting diffused heat field and on phase contrast results of changing the size of the crack, its shape, its position (buried depth and inclination), and the position of the 3D source.

2. Methods

2.1 Problem definition

This work simulates the three-dimensional heat diffusion in the vicinity of a 3D crack, generated by a point heat source, as illustrated in Figure 1. The medium is an unbounded spatially uniform solid medium of density ρ, thermal conductivity λ and specific heat c. The crack, with surface S, is assumed to have null thickness. Null heat fluxes are prescribed along the surface.

This system is subjected to a point heat source placed at (x_s, y_s, z_s),

$$\hat{f}(x, y, z, t) = P\delta(x - x_s)\delta(y - y_s)\delta(z - z_s)e^{i\omega t} \tag{1}$$

where $\delta(x - x_s)$, $\delta(y - y_s)$ and $\delta(z - z_s)$ are Dirac-delta functions, and ω is the frequency of the source. The response of this heat source can be given by the expression:

$$T_{\text{inc}}(x, y, z, x_s, y_s, z_s, \omega) = \frac{Pe^{-i\sqrt{\frac{i\omega}{K}}r_0}}{2\lambda r_0} \tag{2}$$

in which K is the thermal diffusivity defined by $\dfrac{\lambda}{\rho c}$, ω is the oscillating frequency, $i = \sqrt{-1}$, $r_0 = \sqrt{(x - x_s)^2 + (y - y_s)^2 + (z - z_s)^2}$ and P is the amplitude of the heat source.

2.2 The normal-derivative integral equation (TBEM)

The transient heat transfer by conduction is governed by the diffusion equation:

$$\left(\frac{\partial^2}{\partial x^2} + \frac{\partial^2}{\partial y^2} + \frac{\partial^2}{\partial z^2}\right)T(\boldsymbol{x}, \omega) + (k_c)^2 T(\boldsymbol{x}, \omega) = 0 \tag{3}$$

in which $\boldsymbol{x} = (x, y, z)$ and $k_c = \sqrt{\dfrac{-i\omega}{K}}$.

The classical boundary integral equation, formulated in the frequency domain, is:

$$b\,T(\boldsymbol{x}_0,\omega) = -\int_S H(\boldsymbol{x},\mathbf{n}_{n1},\boldsymbol{x}_0,\omega)\,T(\boldsymbol{x},\omega)\,\mathrm{d}s + T_{\mathrm{inc}}(\boldsymbol{x}_0,\boldsymbol{x}_s,\omega) \qquad (4)$$

where H are the fundamental solutions (Green's functions) for the heat fluxes, at a point $\boldsymbol{x} = (x, y, z)$ on the boundary of the surface S, due to a virtual point heat source at $\boldsymbol{x}_0 = (x_0, y_0, z_0)$; $\mathbf{n}_{n1}$ represents the unit outward normal along the boundary S, at $\boldsymbol{x} = (x, y, z)$; b is a constant defined by the shape of the boundary, taking the value $1/2$ if $\boldsymbol{x}_0 = (x_0, y_0, z_0) \in S$, and 1 otherwise.

The required Green's functions for heat flux in an unbounded medium, in Cartesian coordinates, are given by:

$$H\left(\boldsymbol{x},\mathbf{n}_{n1},\boldsymbol{x}_0,\omega\right) = \frac{\mathrm{e}^{-ik_c r}\left(-ik_c r - 1\right)}{4\lambda\pi r^2}\frac{\partial r}{\partial \mathbf{n}_{n1}} \qquad (5)$$

with $r = \sqrt{\left(x - x_0\right)^2 + \left(y - y_0\right)^2 + \left(z - z_0\right)^2}$.

The normal-derivative integral equation can be derived by applying the gradient operator to the boundary integral equation (4), which can be seen as assuming the existence of dipole heat sources. When the boundary of the inclusion is loaded with dipoles (dynamic doublets) the required integral equations can be expressed as:

$$a\,T(\boldsymbol{x}_0,\omega) = -\int_S \overline{H}(\boldsymbol{x},\mathbf{n}_{n1},\mathbf{n}_{n2},\boldsymbol{x}_0,\omega)\,T(\boldsymbol{x},\omega)\,\mathrm{d}s + \overline{T}_{inc}(\boldsymbol{x}_0,\mathbf{n}_{n2},\boldsymbol{x}_s,\omega) \qquad (6)$$

The Green's functions $\overline{H}$ are defined by applying the gradient operator to H, which can be seen as the derivatives of these former Green's functions, to obtain heat fluxes. In these equations, $\mathbf{n}_{n2}$ is the unit outward normal to the boundary S at the collocation points $\boldsymbol{x}_0 = (x_0, y_0, z_0)$, defined by the vector $\mathbf{n}_{n2}$. In this equation, the factor a is null for piecewise planar boundary elements.

The required three-dimensional Green's functions for an unbounded space are now defined as:

$$\overline{H}(\boldsymbol{x},\mathbf{n}_{n1},\mathbf{n}_{n2},\boldsymbol{x}_0,\omega) = \frac{\partial H}{\partial x}\frac{\partial x}{\partial \mathbf{n}_{n2}} + \frac{\partial H}{\partial y}\frac{\partial y}{\partial \mathbf{n}_{n2}} + \frac{\partial H}{\partial z}\frac{\partial z}{\partial \mathbf{n}_{n2}} \qquad (7)$$

with

$$\frac{\partial H}{\partial x}(\boldsymbol{x},\mathbf{n}_{n1},\mathbf{n}_{n2},\boldsymbol{x}_0,\omega) = \frac{1}{4\pi}\left\{ A\left[\left(\frac{\partial r}{\partial x}\right)^2\frac{\partial x}{\partial \mathbf{n}_{n1}} + \frac{\partial r}{\partial x}\frac{\partial r}{\partial y}\frac{\partial y}{\partial \mathbf{n}_{n1}} + \frac{\partial r}{\partial x}\frac{\partial r}{\partial z}\frac{\partial z}{\partial \mathbf{n}_{n1}}\right] + B\left[\frac{\partial x}{\partial \mathbf{n}_{n1}}\right]\right\} ,$$

$$\frac{\partial H}{\partial y}(\boldsymbol{x},\mathbf{n}_{n1},\mathbf{n}_{n2},\boldsymbol{x}_0,\omega) = \frac{1}{4\pi}\left\{ A\left[\frac{\partial r}{\partial x}\frac{\partial r}{\partial y}\frac{\partial x}{\partial \mathbf{n}_{n1}} + \left(\frac{\partial r}{\partial y}\right)^2\frac{\partial y}{\partial \mathbf{n}_{n1}} + \frac{\partial r}{\partial y}\frac{\partial r}{\partial z}\frac{\partial z}{\partial \mathbf{n}_{n1}}\right] + B\left[\frac{\partial y}{\partial \mathbf{n}_{n1}}\right]\right\} ,$$

$$\frac{\partial H}{\partial z}(\boldsymbol{x},\mathbf{n}_{n1},\mathbf{n}_{n2},\boldsymbol{x}_0,\omega) = \frac{1}{4\pi}\left\{ A\left[\frac{\partial r}{\partial x}\frac{\partial r}{\partial z}\frac{\partial x}{\partial \mathbf{n}_{n1}} + \frac{\partial r}{\partial y}\frac{\partial r}{\partial z}\frac{\partial y}{\partial \mathbf{n}_{n1}} + \left(\frac{\partial r}{\partial z}\right)^2\frac{\partial z}{\partial \mathbf{n}_{n1}}\right] + B\left[\frac{\partial z}{\partial \mathbf{n}_{n1}}\right]\right\} ,$$

$$A = -\frac{k_c^2\,\mathrm{e}^{-ik_c r}}{r} + \frac{3ik_c\,\mathrm{e}^{-ik_c r}}{r^2} + \frac{3\mathrm{e}^{-ik_c r}}{r^3} \quad \text{and} \quad B = -\frac{ik_c\,\mathrm{e}^{-ik_c r}}{r^2} - \frac{\mathrm{e}^{-ik_c r}}{r^3} .$$

In Equation (6) the incident heat field is computed as

$$\overline{T}_{inc}(\boldsymbol{x}, \mathbf{n}_{n2}, \boldsymbol{x}_s, \omega) = \frac{\mathrm{Pe}^{-\mathrm{i}k_c r_0}\left(-\mathrm{i}k_c r_0 - 1\right)}{2r_0^2}\left(\frac{\partial r_0}{\partial x}\frac{\partial x}{\partial \mathbf{n}_{n2}} + \frac{\partial r_0}{\partial y}\frac{\partial y}{\partial \mathbf{n}_{n2}} + \frac{\partial r_0}{\partial z}\frac{\partial z}{\partial \mathbf{n}_{n2}}\right) \quad (8)$$

The global solution is found by solving Eq. (6), which requires the discretization of the interface S into N planar boundary elements, with one nodal point in the middle of each element. The integrations in Eq. (6) are evaluated using a Gaussian quadrature scheme when the element to be integrated is not the loaded element. For the loaded element (the hypersingular element), however, the integrands exhibit a singularity and the integration can be carried out in closed form, as defined by Tadeu *et al.* [14].

The proposed algorithm was verified using a circular cylindrical cavity for which analytical solutions are known. The results showed good approximation between the responses calculated analytically and those given by the BEM formulation, and the solution improved for higher numbers of boundary elements. This verification is not given here for reasons of space.

3. Results and discussion

3.1 Case studies

The applicability and usefulness of the proposed approach are illustrated by simulating the heat propagation around a 3D null thickness crack hosted in an unbounded solid medium and computing the phase-contrast images of the resulting heat wave. Various parameters are changed for the study of the influence of the properties of the plane crack S (see Figure 2) on heat diffusion and phase image computations. The parameters changed are the shape of the crack, its size, position and distance from the heat source and to the surface (grid of receivers).

Initially, the crack is parallel to the yz plane and the 3D point source is located at its origin $(x_s, y_s, z_s) = (0.0\,\text{m}, 0.0\,\text{m}, 0.0\,\text{m})$. Computations are performed over three fine grids of receivers. Two grids are placed at a distance from the source, along the x axis: grid G1 is $0.0675\,\text{m}$ from the crack and is placed over a plane at $x = 0.5325\,\text{m}$, and grid G2 is placed over the plane at $x = 0.6725\,\text{m}$. The third grid of receivers, G3, is parallel to the z axis over the plane located at $z = 0.0\,\text{m}$. The receivers were spaced at equal intervals of $0.005\,\text{m}$, $0.00625\,\text{m}$ and $0.006\,\text{m}$ in the x, y and z axis direction, respectively. The grid of receivers G1 simulates an object's surface on which thermographic data given by IRT is recorded.

Three different geometries are simulated in order to study the influence of the size of the crack (see figure 3b). Additionally, a $0.05 \times 0.2\,\text{m}^2$ crack is modeled to study the influence of changing the shape of the crack. The crack is initially placed at $x = 0.6\,\text{m}$. Changes produced when the crack is closer to the simulated object's surface were studied by moving the grid of receivers $0.04\,\text{m}$ closer to the crack. The influence of changing the distance from source to defect was studied by moving the source to $x = 0.4525\,\text{m}$. The influence of the crack inclination was studied by tilting the vertical crack around an axis parallel to the z axis, by $\alpha = 15°$ and $\alpha = 40°$ (see figure 3a). Results are analyzed for specific receivers placed at the center and the extremities of the cracks, as shown in figure 3b. Responses are also computed for the example of an infinite sized crack with null heat fluxes (labeled REF) by applying an image source technique.

3.2 Simulation results of heat field in the time domain and thermal wave phase

The heat field in the time domain was determined by applying a numerical inverse fast Fourier transform in the frequency domain. Aliasing phenomena are dealt by introducing complex frequencies with a small imaginary part, taking the form $\omega_c = \omega - \mathrm{i}\eta$ (where $\eta = 0.7\Delta\omega$, and $\Delta\omega$ is the frequency step), following the technique described in [15].

The thermal properties of the host medium are those of concrete: $c = 880$ J.kg^{-1}.°C^{-1}, ρ=2300 kg.m^{-3} and $\lambda = 1.40$ W.m^{-1}.°C^{-1}. All the calculations are performed in the $\left[0.0, 1.024 \times 10^{-3}\right]$ Hz frequency range, with an increment of $\Delta f = 0.5 \times 10^{-6}$ Hz, resulting in a $1/\left(0.5 \times 10^{-6}\right)$ s total time window for the analysis. The upper limit of the frequency range was defined so as to ensure a negligible contribution to the responses. Responses for higher frequencies would have a null contribution. The imaginary part of the frequency is given by $\eta = 0.7 \times 2\pi \Delta f$. The host medium is assumed to be initially at 20.0 °C. The source starts emitting energy at instant $t = 0.5$ h and it continues for 1.5 h. The heat source time dependence is assumed to be rectangular with an amplitude of $P = 154.5$. This amplitude was defined so that a maximum temperature increase of 15.0 °C is registered at REC A.

The effects of the presence of a defect on the temperature diffusion pattern, computations were studied for a medium without any cracks and a medium with an embedded crack. The difference between the two results expresses the differences in temperature that can be used by IRT in defect detection. Figure 4 illustrates the time domain snapshots of the temperature distribution at $t = 20$ h for a 0.2×0.2 m^2 vertical crack placed at $x = 0.6$ m, subjected to a 3D point source placed at the origin, on the three grids of receivers placed at $x_{G1} = 0.5325$ m, $x_{G2} = 0.6725$ m and $z_{G3} = 0.0$ m.

Thermal wave phase results are computed directly in the frequency domain, assuming the existence of harmonic sources with unitary amplitude. This corresponds to an ideal Dirac pulse in the time domain, which has an infinite flat spectrum in the frequency domain. Phase-contrast images are obtained by computing the difference between the phase of the heat waves within the medium when the crack is embedded in the medium and for the medium without any defects.

Figure 5 illustrates the phase-contrast curve obtained at REC A. The resulting curve shows a clearly defined peak in the frequency spectra at maximum phase-contrast $\left|\Delta\phi_{max}\right|$, which corresponds to the characteristic frequency f_{ch} used in defect detection. The detection threshold is given by the blind frequency f_b at zero phase-contrast. Figure 5 also makes it clear that an infinitely sized crack leads to lower characteristic frequency f_{ch}.

3.2.1 Influence of crack size

The following graphs show the phase contrast curves obtained for four different crack sizes: 0.3×0.3 m^2; 0.2×0.2 m^2; 0.1×0.1 m^2 and 0.05×0.2 m^2 at receivers REC A, REC B, REC C and REC D.

The results show that, at all receivers, the characteristic frequency f_{ch} decreases and the corresponding maximum phase-contrast absolute value $\left|\Delta\phi_{max}\right|$ increases, for larger crack sizes. It can be seen that increasing the size of the crack leads to results closer to the reference curve, which was expected since the larger the crack the closer it gets to the behavior of an infinite size crack. In no case does the blind frequency f_b change significantly and the detection threshold does not change much with crack size variation. The phase-contrast response is significantly reduced when the receivers are placed beyond the crack limits, as shown in Figure 6c for REC C (placed outside the limits of the 0.1×0.1 m^2 crack) and in Figure 6d for REC D (placed outside the limits of the 0.1×0.1 m^2, 0.05×0.2 m^2 and 0.2×0.2 m^2 cracks). For any crack size, when receivers are located further from the center of the crack there is a decrease in the f_{ch} values. It is also seen that the amplitude of the phase-contrast decreases when the geometry of the crack changes from 0.1×0.1 m^2 to 0.05×0.2 m^2 (see Figures 6a and 6b).

Figure 7 contains snapshots of the phase-contrast images computed along the grid of receivers G1, for three different crack sizes. The snapshots are taken at the frequency f_{ch} which is the maximum

phase-contrast $\left|\Delta\phi_{max}\right|$ observed in receiver REC A, located at the center of each crack (indicated in these plots by a round red mark). The phase-contrast snapshots clearly demonstrate the ability to detect the presence of the crack and to assess its size. It is clearly seen that outside the crack limits the phase-contrast tends to zero because the effect of the reflected heat field is diminished.

3.2.2 Influence of source position

The graphs in Figure 8 illustrate the influence of changing the source position and show the phase-contrast results obtained when the source is moved from the origin to a position closer to the defect, to $x = 0.4525\,\text{m}$, so that the distance from the source to the defect is reduced from $0.6\,\text{m}$ to $0.1475\,\text{m}$.

The blind frequency f_b does not suffer significant alteration in any of the cases. When the distance is shorter there is a decrease in the characteristic frequency f_{ch} value in REC A, and a decrease in the corresponding maximum phase-contrast absolute value $\left|\Delta\phi_{max}\right|$. However, in REC C there is an increase in both the f_{ch} and $\left|\Delta\phi_{max}\right|$. The reference curves in Figure 8b show that changing the source position gives different results depending on the position of the receiver, and that it has significant importance on the peak phase-contrast value, especially for receivers closer to the center of the crack. For both cracks ($0.2\times0.2\,\text{m}^2$ and infinite) the characteristic frequency increases the further the receiver is from the center.

3.2.3 Influence of crack depth

The grid of receivers G1 is shifted along the x axis to study the influence of the depth of the defect. The graphs in Figure 9a show the phase-contrast results obtained from modeling a $0.2\times0.2\,\text{m}^2$ crack for receivers placed at $x_{G1} = 0.5325\,\text{m}$ (REC A and REC C) and at $x_{G1} = 0.5725\,\text{m}$ (REC A' and REC C'), simulating a defect depth reduction. Figure 9b shows the reference curves for the same positions.

For both sizes results show that reducing the depth of the defect increases the f_{ch} and the corresponding $\left|\Delta\phi_{max}\right|$. Furthermore, as the buried depth is lessened the detection threshold given by the blind f_b frequency also increases. The reference curves in Figure 9b show that for an infinite size crack the position of the receivers on the grid does not influence results.

The resulting curves are analyzed further, aiming to investigate the relationship between the depth of the defect and the characteristic frequency. The results shown in Table 1 relate to the product of the square of the defect depth d^2 and the characteristic frequency f_{ch} recorded at the receivers placed at $x_{G1} = 0.5725\,\text{m}$ (REC A' to E'), for a defect depth of $d = 0.0275\,\text{m}$, and those originally placed at $x_{G1} = 0.5325\,\text{m}$ (REC A to E), corresponding to an initial defect depth of $d = 0.0675\,\text{m}$.

It can be seen that fairly similar results are obtained for an infinite sized crack. In this case, the relationship between the depth of the defect d and the characteristic frequency f_{ch} can be approximately expressed by the equation given by Arndt for Civil Engineering applications of square-pulse thermography [16]:

$$d = k_c \times \sqrt{K\!\big/\!f_{ch}} \qquad (9)$$

where k_c is a correction factor dependant on the thermal properties of the medium, K is the thermal diffusivity as defined previously and f_{ch} is the characteristic frequency.

Table 1 shows that results for finite size cracks get closer to those for the infinite size crack the larger the size of the crack. The correlation between d and f_{ch} is also closer to the one described in Eq. (9) for shorter defect depths and for receiver readings closest to the center of the defect.

3.2.4 Influence of crack inclination

The snapshots in Figure 10 show the phase-contrast image results along G1 for three different crack positions: $\alpha = 0^\circ$, $\alpha = 15^\circ$ and $\alpha = 40^\circ$. The snapshots are taken at the frequencies corresponding to maximum phase-contrast in receivers REC E and REC F.

The images show that as the crack is tilted the peak phase-contrast occurs at higher frequencies and phase-contrast amplitude is reduced at lower frequencies. Furthermore, as seen for $\alpha = 40^\circ$, in the low frequency spectrum the response is inverted and a positive difference is recorded in receivers located in front of the lower part of the crack. In these receivers the peak phase-contrast occurs for high f_{ch} values, which is agrees with the results described in the previous section (reducing the depth of the defect increases f_{ch} and $\left|\Delta\phi_{\max}\right|$ values). However, as the crack is tilted further, the lower part of the defect gets closer to the surface and the upper part gets further away, which leads to a mixed response. As shown by the images for $\alpha = 40^\circ$, conclusions regarding the size and shape of the crack can no longer be deduced by the phase-contrast image given at a specific frequency. We have to sweep a wide range of frequencies to fully assess the size and shape of the defect.

To better understand these results, the heat field in the time domain is computed via an inverse fast Fourier transform applied in the frequency domain and by assuming the source time evolution defined previously. Computations are performed for a medium without any cracks and a medium with the embedded $0.2 \times 0.2 \text{ m}^2$ cracks. Figure 11 shows snapshots of the temperature differences between both results at different time instants ($t = 10 \text{ h}$, $t = 20 \text{ h}$ and $t = 30 \text{ h}$) for different angles $\alpha = 0^\circ$, $\alpha = 15^\circ$ and $\alpha = 40^\circ$.

Given the distance from the crack to the grid of receivers on $x = 0.5325 \text{ m}$, the temperature field is very mild for all cases. Results show that at $t = 10 \text{ h}$ the temperature is still increasing, while at $t = 30 \text{ h}$ the source has already been turned off for a long time and the temperature is falling. The temperature field recorded on the perpendicular grid G3 bears out this behavior (see figure 2).

The temperature field is progressively weaker as the crack is tilted for the receivers in front of the upper part of the defect while it is stronger for the lower receivers. This is particularly noticeable at $t = 10 \text{ h}$. When the crack is tilted horizontally the temperature difference is null (not shown), because the crack is aligned with the point heat source at $z = 0$. In this specific case IRT analysis will not be able to detect the defect.

4. Conclusions

In this paper the authors have proposed a three-dimensional normal-derivative integral equation (TBEM) formulation to allow heat conduction modeling in the vicinity of cracks embedded in an unbounded medium for applications using active IRT for defect detection. The hypersingular integrals that appear when the element to be integrated is the loaded one (singular element) are integrated analytically. Our model is applicable to any medium that can be deemed homogeneous and where the heat conduction phenomena can be governed by the Helmholtz equation. Such media may include steel, concrete, mortar, rock, polymers, etc.

The proposed formulation was employed to simulate the active IRT procedure in a set of numerical examples where a crack is placed in an unbounded space. Parameters which are relevant features in non-destructive testing by active IRT, such as the depth at which the crack is embedded, its size, shape, inclination and distance from the heat source, were analyzed.

Both the temperature differences and the phase-contrast images of the resulting thermal waves were computed by modeling the heat waves within the medium where there is an embedded crack and for the

medium without defects. Numerical results obtained in this study demonstrate that the mentioned crack parameters may have considerable influence on active IRT data results. The numerical simulation results have proven the applicability of the proposed formulation to understanding heat diffusion, in both the time and frequency domains, in the vicinity of 3D defects when subjected to 3D sources. The results were found to be highly influenced by the 3D nature of the crack and heat source. The heat diffusion patterns generated by the proposed models may be found useful for correctly interpreting experimental IRT results as well as for successfully establishing experimental parameters for active IRT testing.

Acknowledgments

References

[1] Maldague X. Theory and Practice of Infrared Technology for Non-destructive Testing. John Wiley & Sons. 2001.

[2] Balaras C A, Argiriou A A. Infrared thermography for building diagnostics. Energy and Buildings 2002; 34: 171-183.

[3] Maierhofer Ch, Arndt R, Röllig M. Influence of concrete properties on the detection of voids with impulse-thermography. Infrared Physics and Technology 2007; 49:213–217.

[4] Maierhofer Ch, Wiggenhauser H, Brink A, Röllig M. Quantitative numerical analysis of transient IR-experiments on buildings. Infrared Physics & Technology 2004; 46 (1-2): 173-180.

[5] Maldague X. Introduction to NDT by Active Infrared Thermography. Materials Evaluation 2002; 6 (9): 1060-1073.

[6] Tartarini P, Corticelli M, Tarozzi L. Dropwise cooling: Experimental tests by infrared thermography and numerical simulations, Applied Thermal Engineering 2009, 29 (7): 1391-1397.

[7] Rodríguez F, Nicolau V. Inverse heat transfer approach for IR image reconstruction: Application to thermal non-destructive evaluation, Applied Thermal Engineering 2012, 33–34: 109-118.

[8] Brebbia C A, Telles J C, Wrobel L C. Boundary Elements Techniques: Theory and Applications in Engineering. Springer-Verlag, Berlin-New York, 1984.

[9] Zhou H, Niu Z, Cheng C, Guan Z. Analytical integral algorithm applied to boundary layer effect and thin body effect in BEM for anisotropic potential problems. Computers & Structures 2008; 86: 1656-1671.

[10] Telles J C F. A self-adaptive co-ordinates transformation for efficient numerical evaluation of general boundary element integrals. International Journal for Numerical Methods in Engineering 1987; 24: 959-973.

[11] Chen X L, Liu Y J. An advanced 3-D boundary element method for characterizations of composite materials. Engineering Analysis with Boundary Elements 2005; 29: 513-523.

[12] Hayami K. Variable transformations for nearly singular integrals in the boundary element method. Publications of the Research Institute for Mathematical Sciences 2005; 41: 821-842.

[13] Ma H, Kamiya N. Distance transformation for the numerical evaluation of near singular boundary integrals with various kernels in boundary element method. Engineering Analysis with Boundary Elements 2002; 26: 329-339.

[14] Tadeu A, Prata J, Simões N. Closed form integration of singular and hypersingular integrals in 3D BEM formulations for heat conduction. Mathematical Problems in Engineering 2012, Article ID 647038, doi:10.1155/2012/647038.

[15] Tadeu A, Simões I, Simões N, Prata J, Simulation of dynamic linear thermal bridges using a boundary element method model in the frequency domain. Energy and Buildings 2011; 43: 3685-3695.

[16] Arndt R W. Square pulse thermography in frequency domain as adaptation of pulsed phase thermography for qualitative and quantitative applications in cultural heritage and civil engineering. Infrared Physics & Technology 2010; 53 (4): 246-253.

Figure 1: 3D geometry of the problem.

Figure 2: 3D view of a 3D null thickness crack hosted in an unbounded solid medium.

Figure 3: Geometry of the systems modelled: a) vertical cross section; b) front view with placement of receivers REC A to REC F.

Figure 4: Snapshots of temperature distribution, in ºC: a) cracked medium; b) medium empty of cracks; c) temperature differences between results in a) and b).

Figure 5: Phase-contrast curves obtained in REC A for a 0.2×0.2 m^2 vertical crack placed at $x = 0.6$ m, and for an infinitely sized crack (curve REF), subjected to a 3D point source at the origin.

Figure 6: Phase-contrast curves obtained for varying crack sizes: a) in REC A $(x = 0.5325\,\text{m}, y = 0.0\,\text{m}, z = 0.0\,\text{m})$; b) in REC B $(x = 0.5325\,\text{m}, y = 0.0\,\text{m}, z = 0.05\text{m})$; c) in REC C $(x = 0.5325\,\text{m}, y = 0.0\,\text{m}, z = 0.1\text{m})$; d) in REC D $(x = 0.5325\,\text{m}, y = 0.0\,\text{m}, z = 0.15\,\text{m})$.

Figure 7: Snapshots of the phase-contrast images $\Delta\phi\,(f)$ obtained at the grid of receivers G1 for different crack sizes.

Figure 8: Phase-contrast curves for results in REC A $(0.5325\,\text{m},\,0.0\,\text{m},\,0.0\,\text{m})$ and REC C $(0.5325\,\text{m},\,0.0\,\text{m},\,0.1\text{m})$ when the heat-source distance is reduced: a) 0.2×0.2 m^2 size crack; b) infinite crack (REF).

Figure 9: Phase-contrast modelling results in REC A , REC C , REC A' , REC C' for: a) 0.2×0.2 m^2 crack; b) infinite crack (REF).

Figure 10: Snapshots of phase-contrast images $\Delta\phi\,(f)$ obtained for different crack positions.

Figure 11: Snapshots of temperature differences for a $0.2 \times 0.2\,\text{m}^2$ crack tilted at different angles.

Table 1: Product between the squared defect depth and the characteristic frequencies recorded at specific receivers.

$d^2 \times f_{ch}$	Crack size			
	$0.1 \times 0.1\,\text{m}^2$	$0.2 \times 0.2\,\text{m}^2$	$0.3 \times 0.3\,\text{m}^2$	REF
REC A	2.51×10^{-7}	1.69×10^{-7}	1.23×10^{-7}	0.57×10^{-7}
REC A'	1.54×10^{-7}	0.87×10^{-7}	0.60×10^{-7}	0.58×10^{-7}
REC E	2.19×10^{-7}	1.69×10^{-7}	1.28×10^{-7}	0.57×10^{-7}
REC E'	1.23×10^{-7}	1.05×10^{-7}	0.71×10^{-7}	0.59×10^{-7}
REC B	2.30×10^{-7}	1.66×10^{-7}	1.25×10^{-7}	0.57×10^{-7}
REC B'	0.06×10^{-7}	0.96×10^{-7}	0.67×10^{-7}	0.58×10^{-7}
REC C	1.85×10^{-7}	1.57×10^{-7}	1.28×10^{-7}	0.59×10^{-7}
REC C'	0.04×10^{-7}	0.89×10^{-7}	0.86×10^{-7}	0.59×10^{-7}
REC D	1.41×10^{-7}	1.30×10^{-7}	1.23×10^{-7}	0.62×10^{-7}
REC D'	0.42×10^{-7}	0.46×10^{-7}	0.86×10^{-7}	0.61×10^{-7}
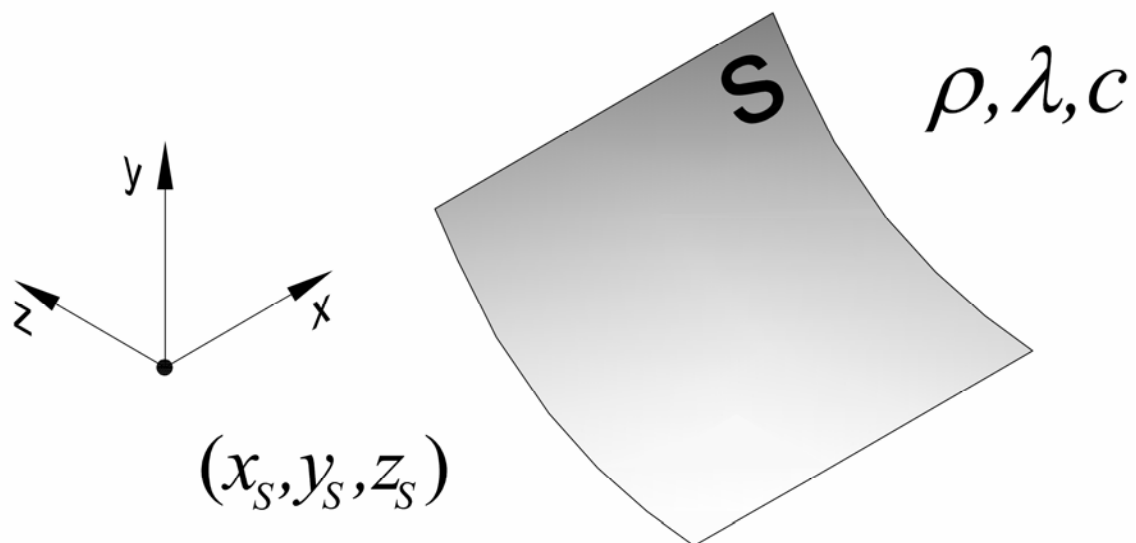
Frequency	$\alpha = 0^o$	$\alpha = 15^o$	$\alpha = 40^o$
$f = 3.30\text{x}10^{-5}\,\text{Hz}$			

$\Delta\phi_{max}^{REC\,E} = -6.97 \times 10^{-3}\ \text{rad}$

$f = 3.75\text{x}10^{-5}\ \text{Hz}$

$\Delta\phi_{max}^{REC\,E} = -5.51 \times 10^{-3}\ \text{rad}$

$f = 4.95\text{x}10^{-5}\ \text{Hz}$

$\Delta\phi_{max}^{REC\,F} = -7.92 \times 10^{-3}\ \text{rad}$

$f = 3.42\text{x}10^{-4}\ \text{Hz}$

$\Delta\phi_{max}^{REC\,F} = -1.00 \times 10^{-1}\ \text{rad}$

$\Delta\phi\ (\text{rad})$ $\Delta\phi\ (\text{rad})$ $\Delta\phi\ (\text{rad})$
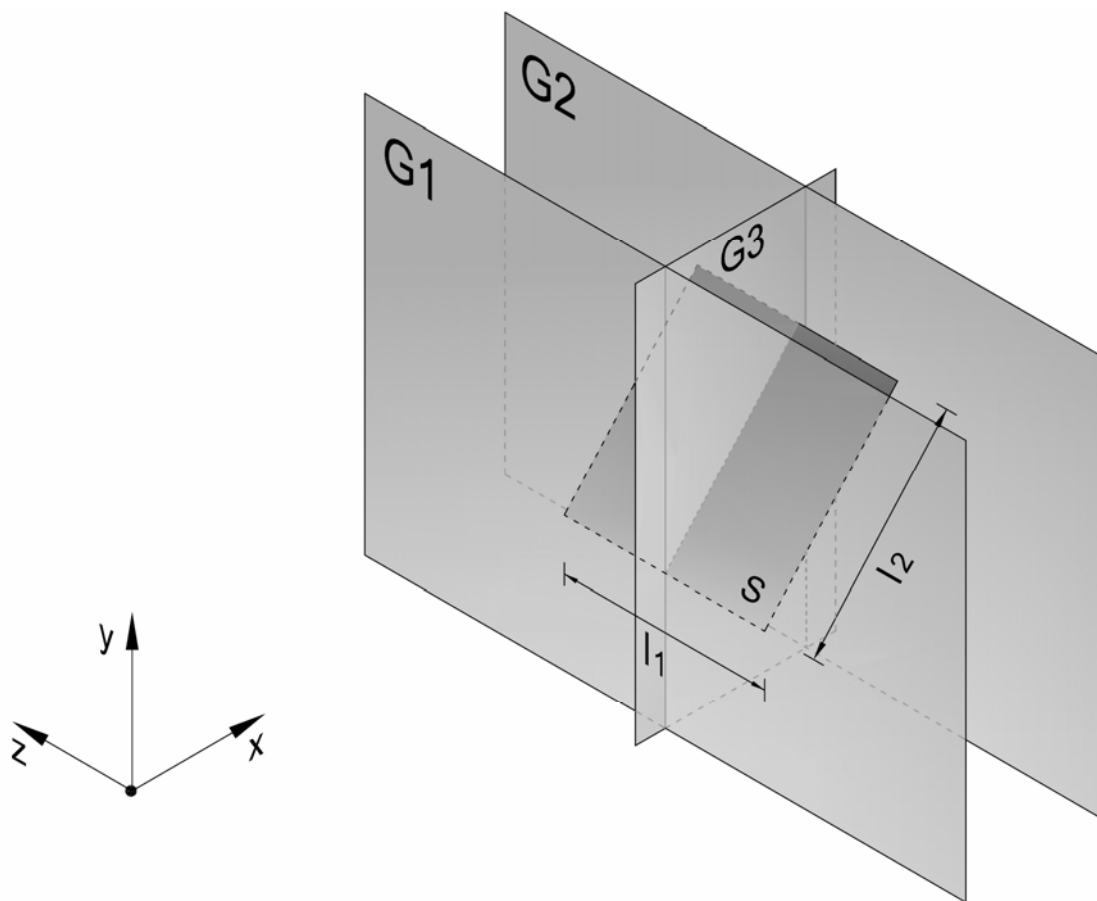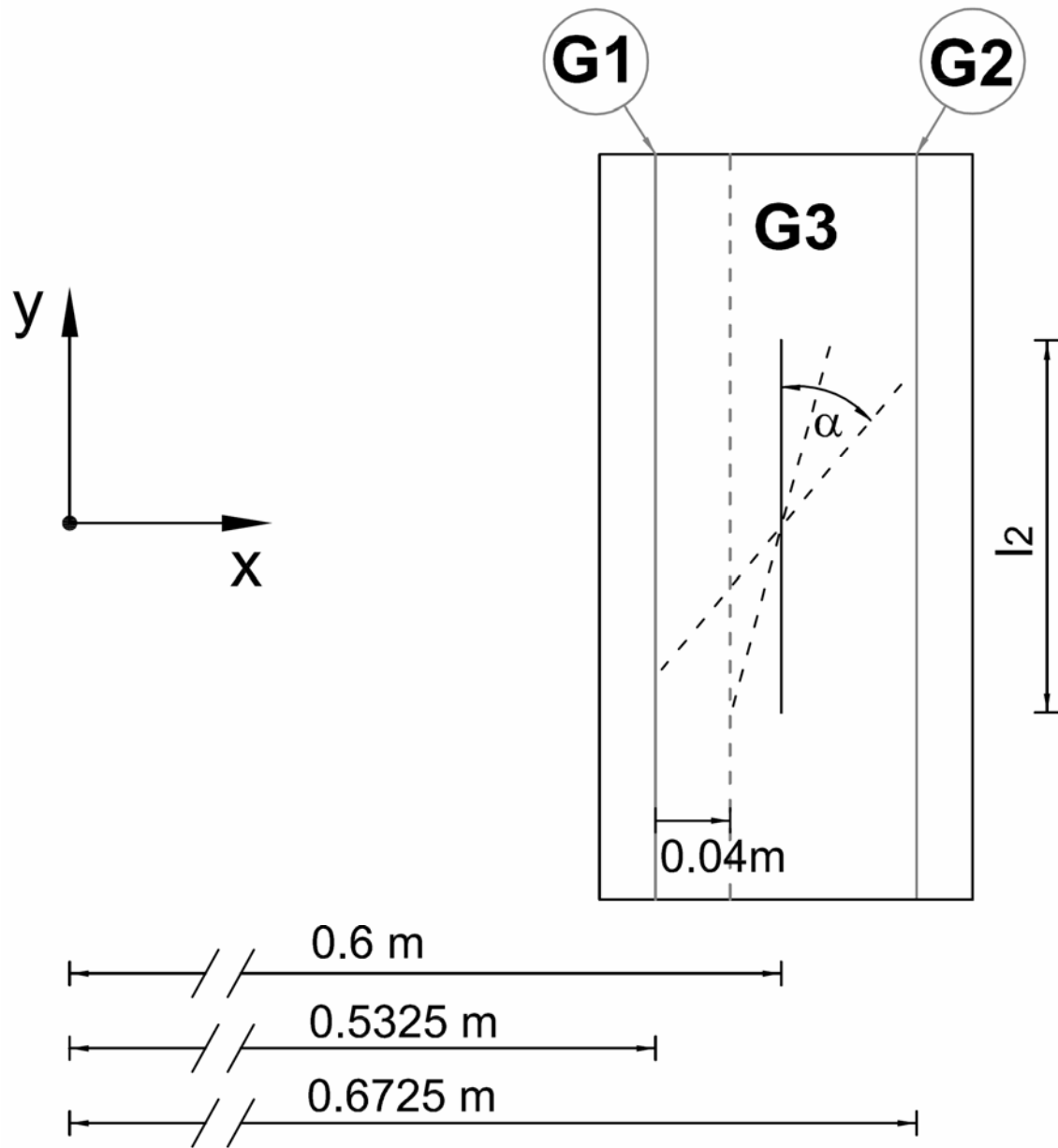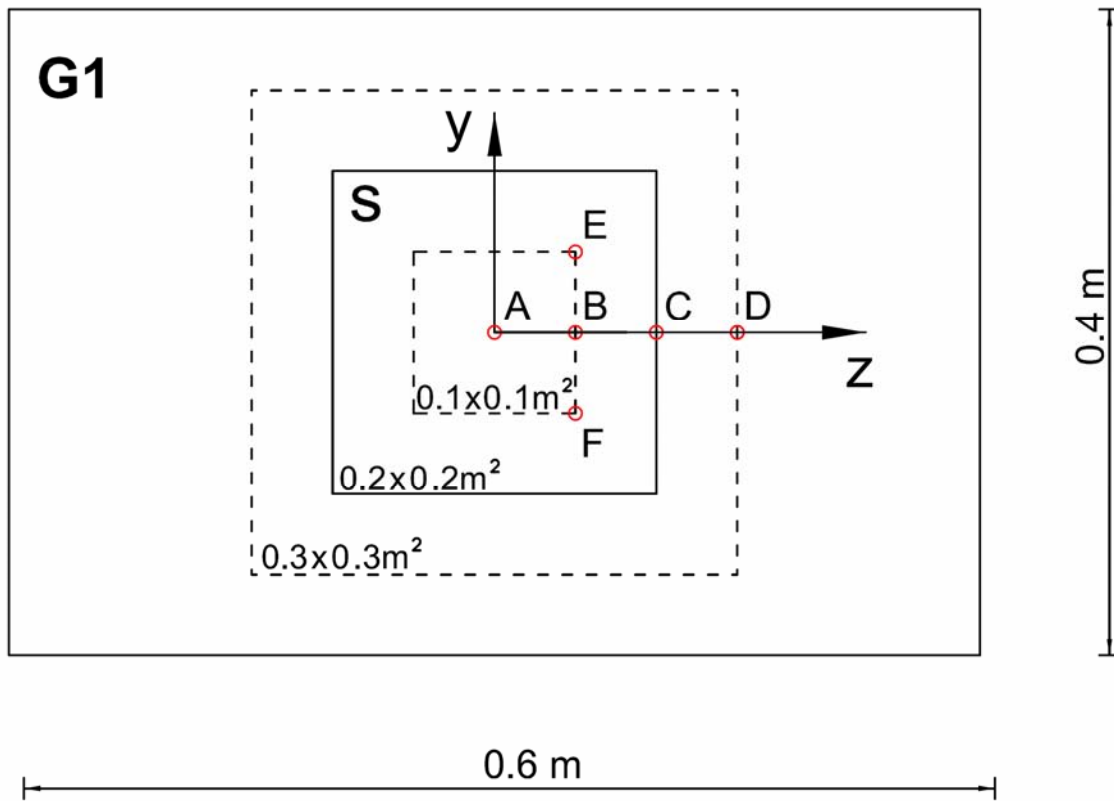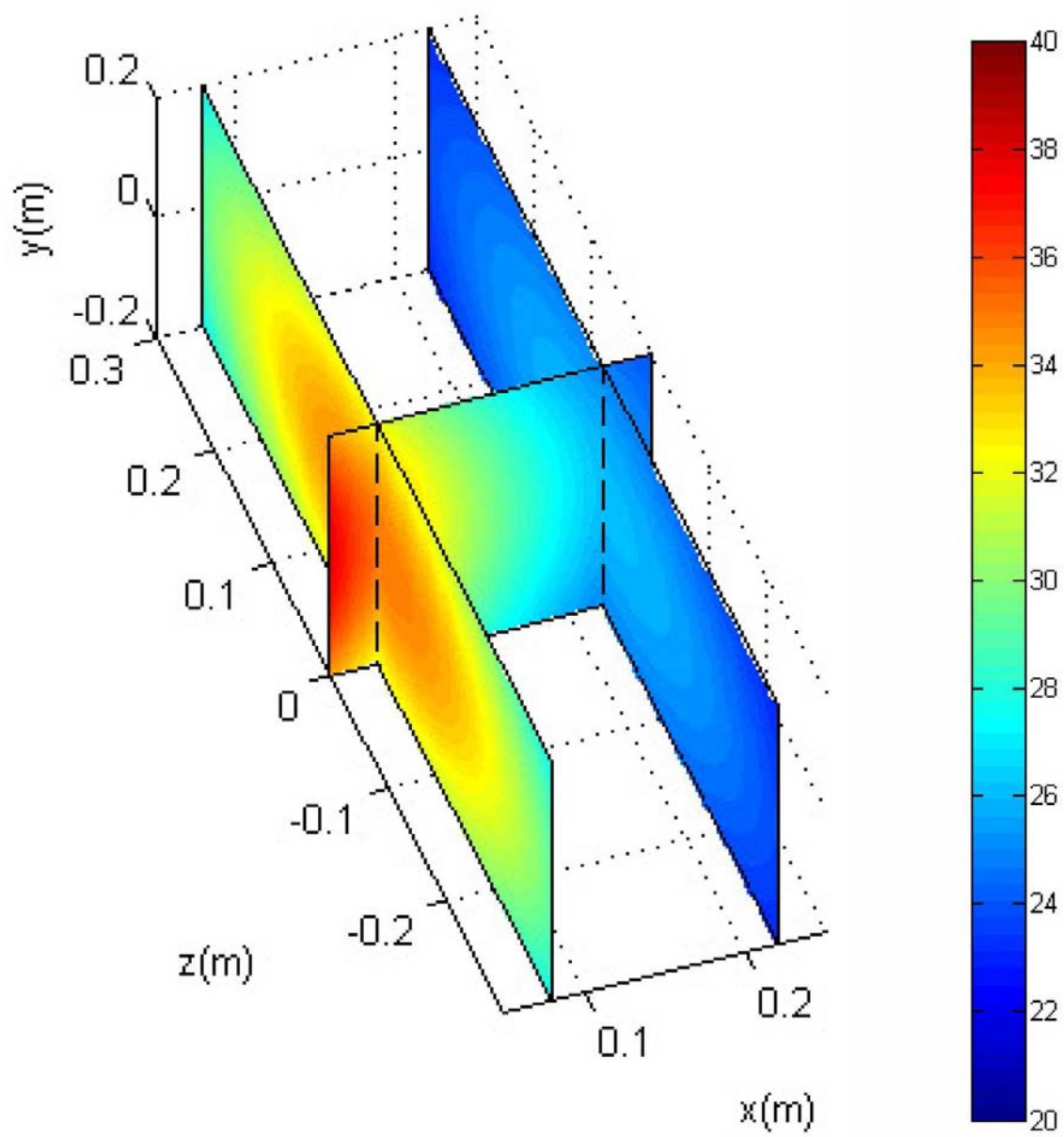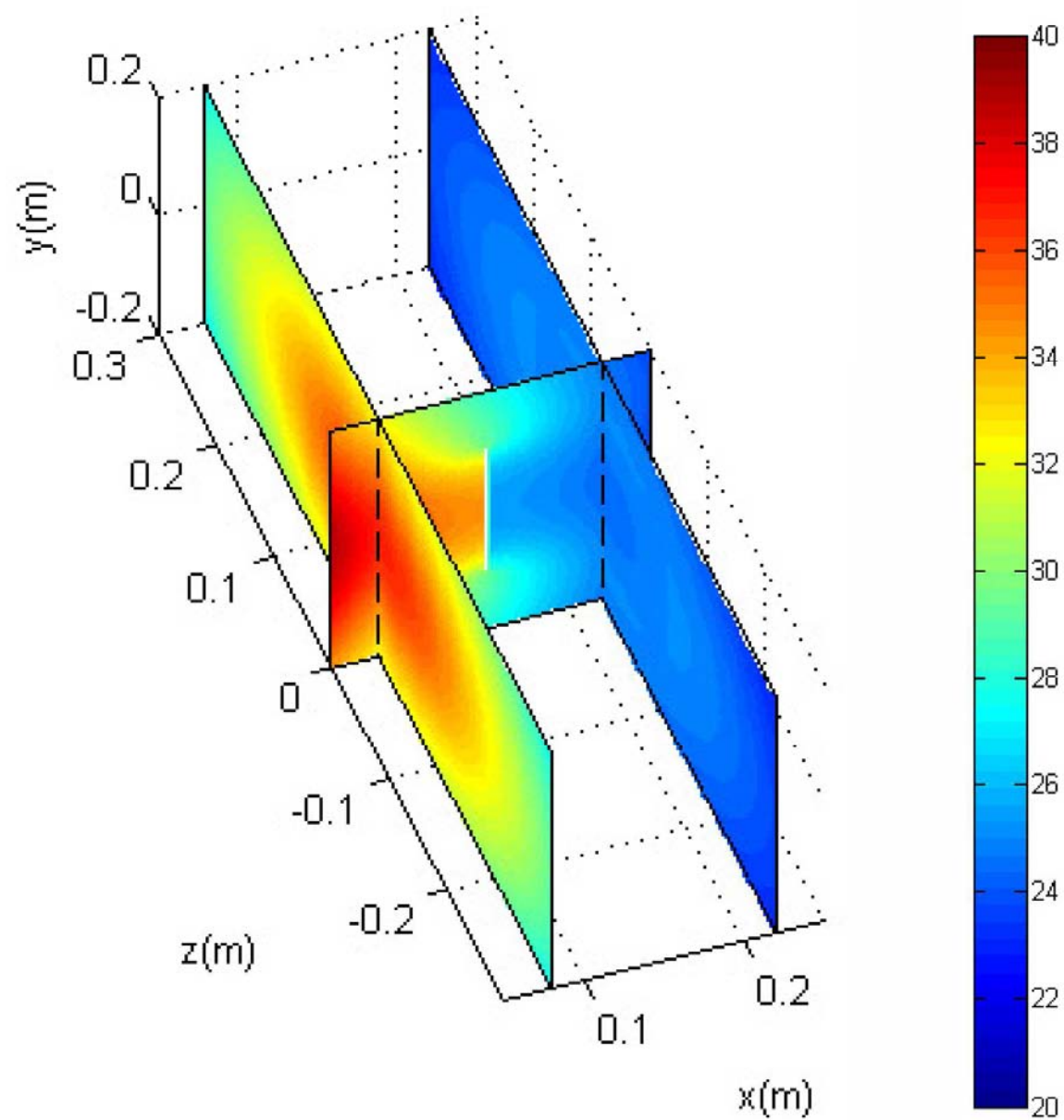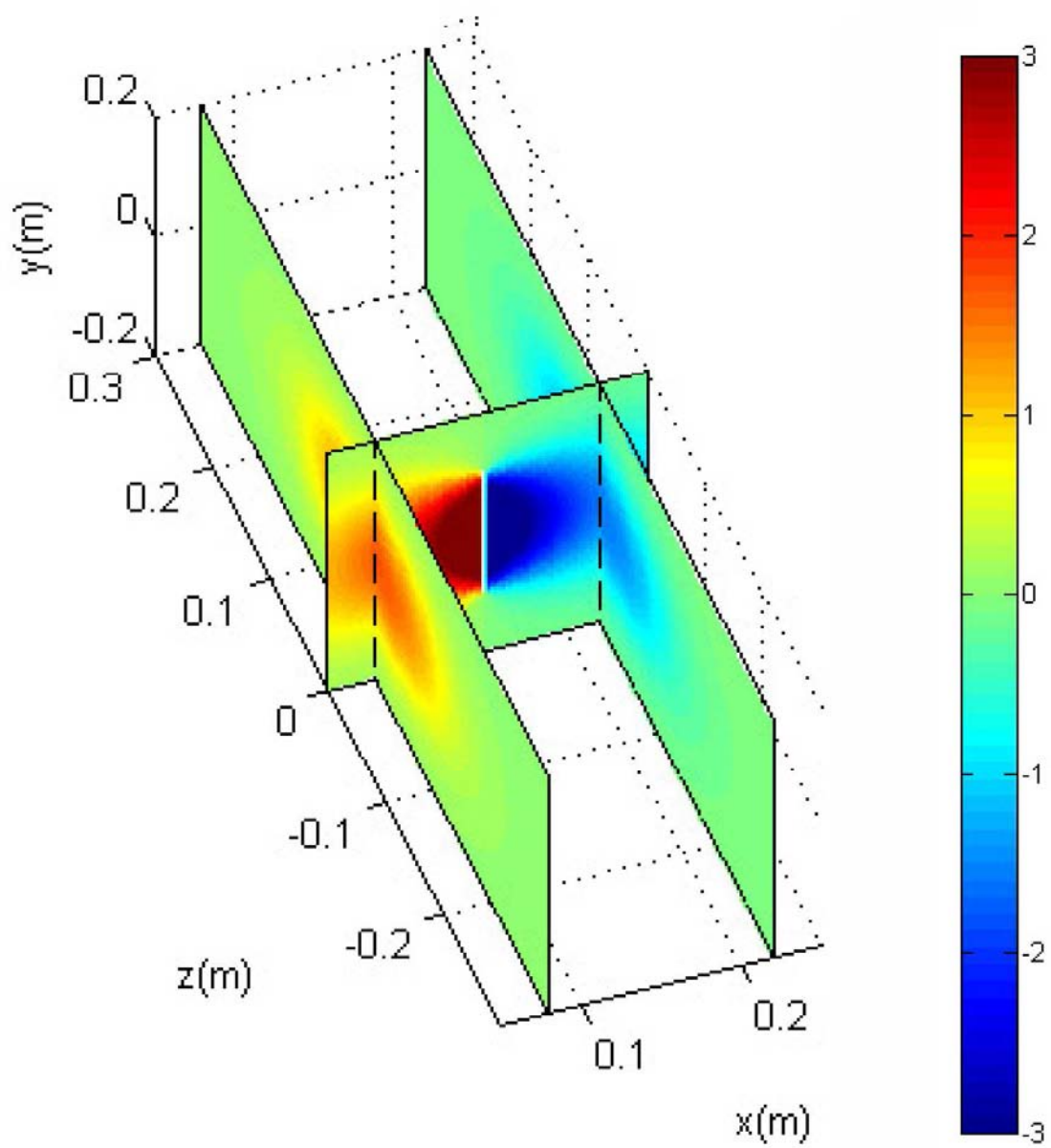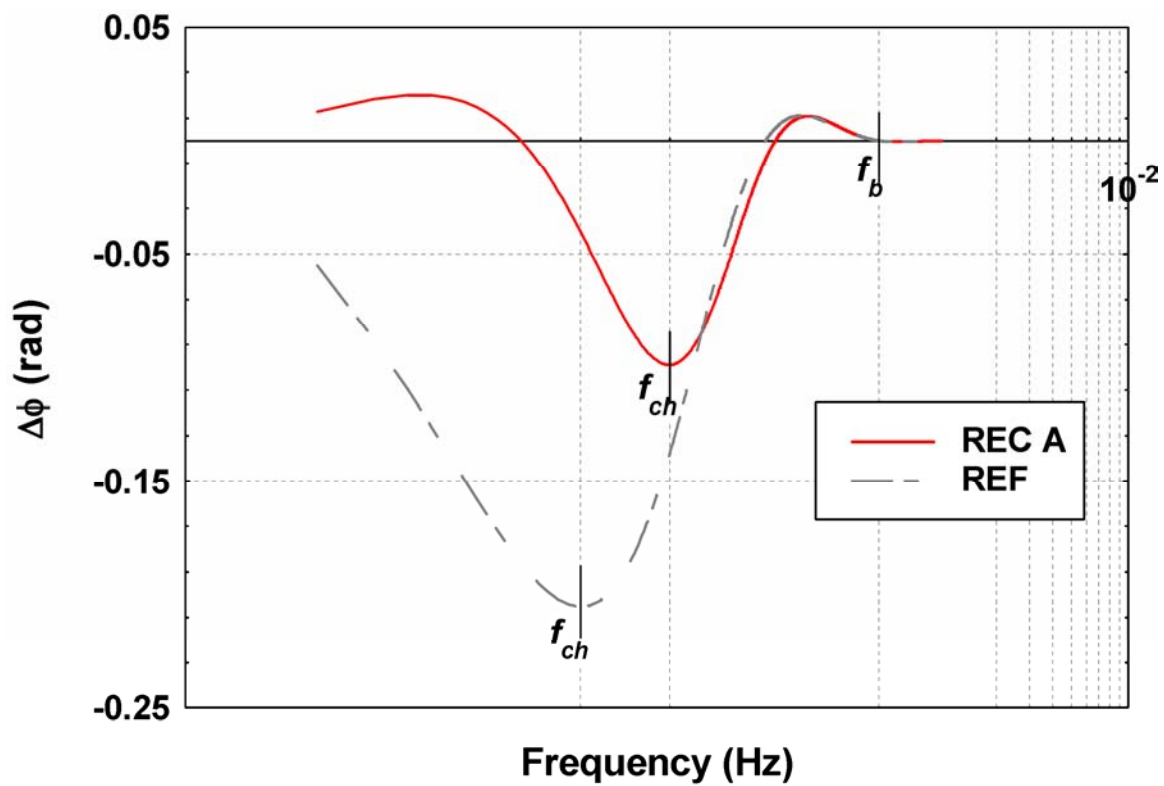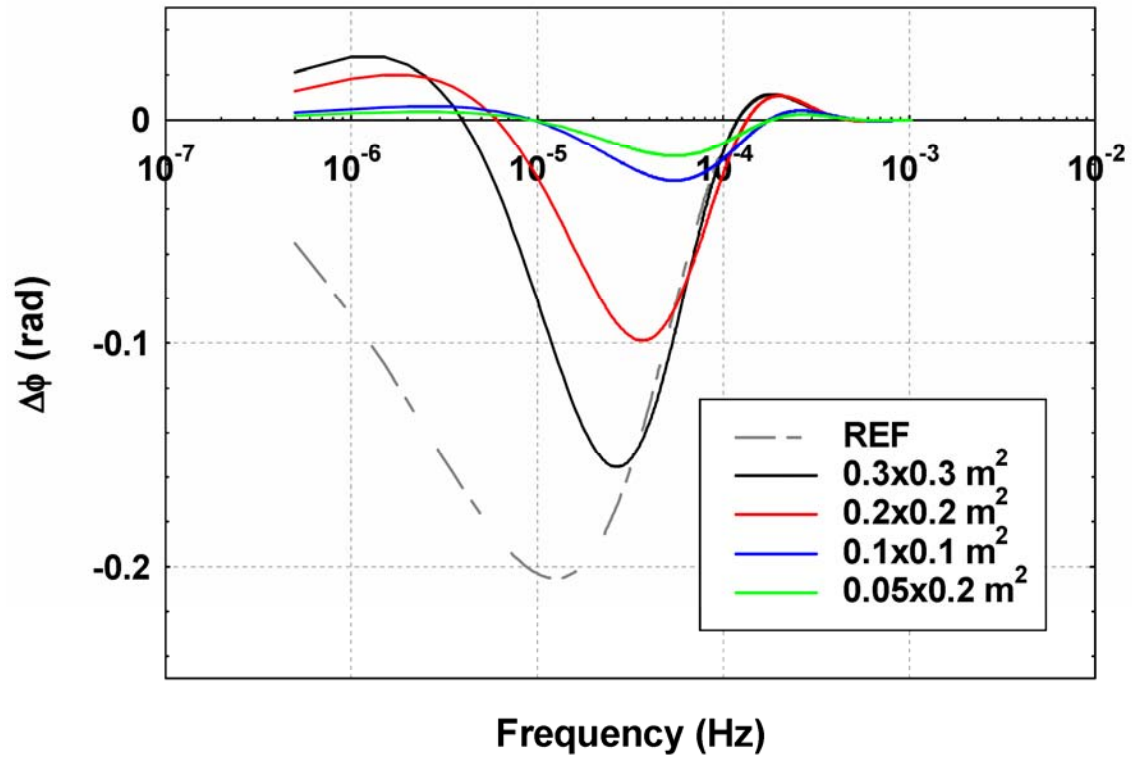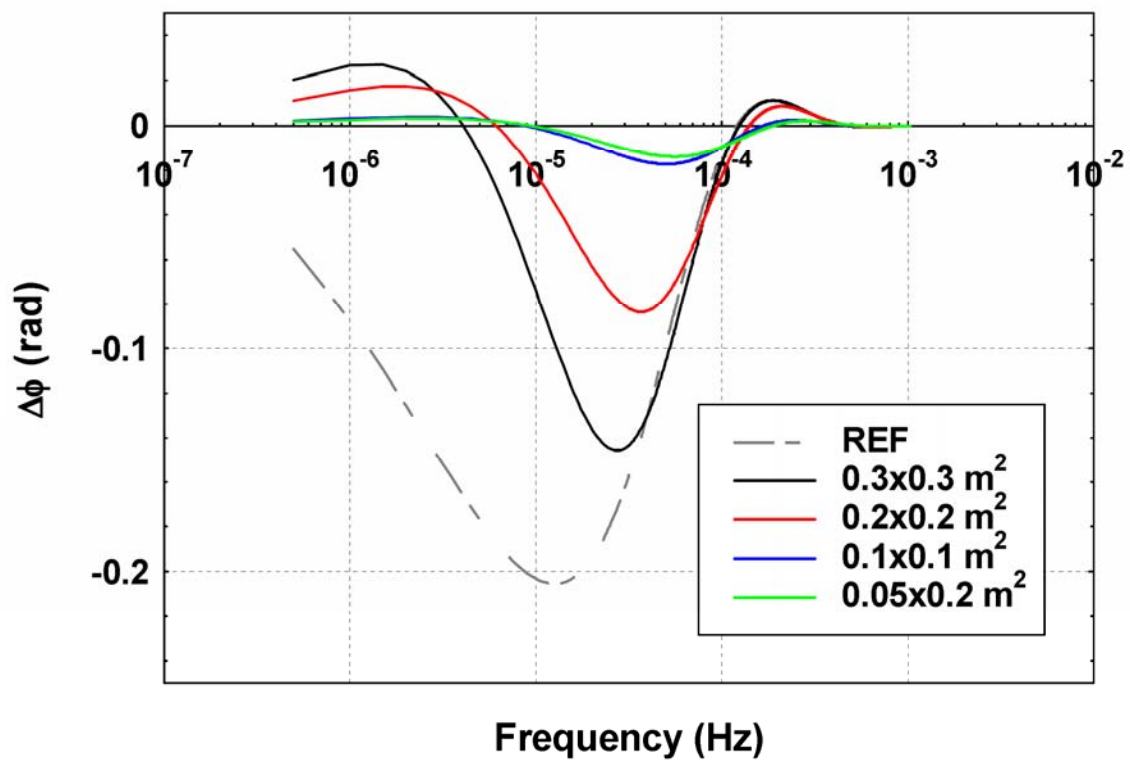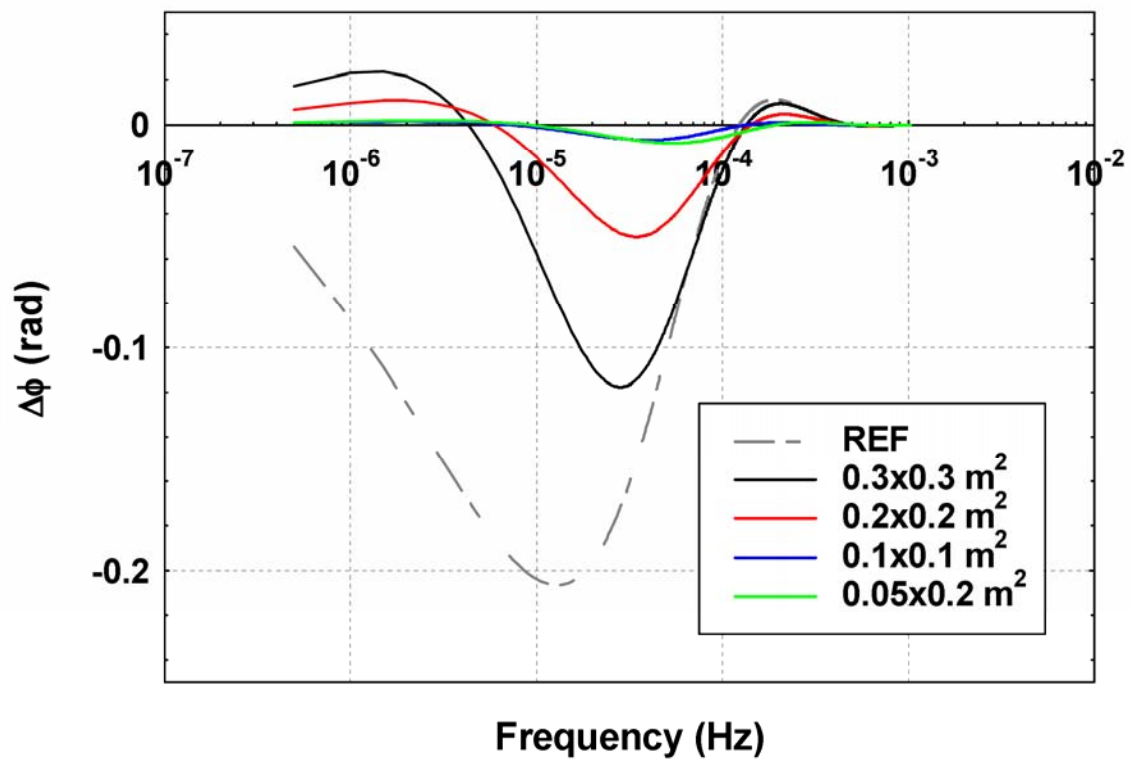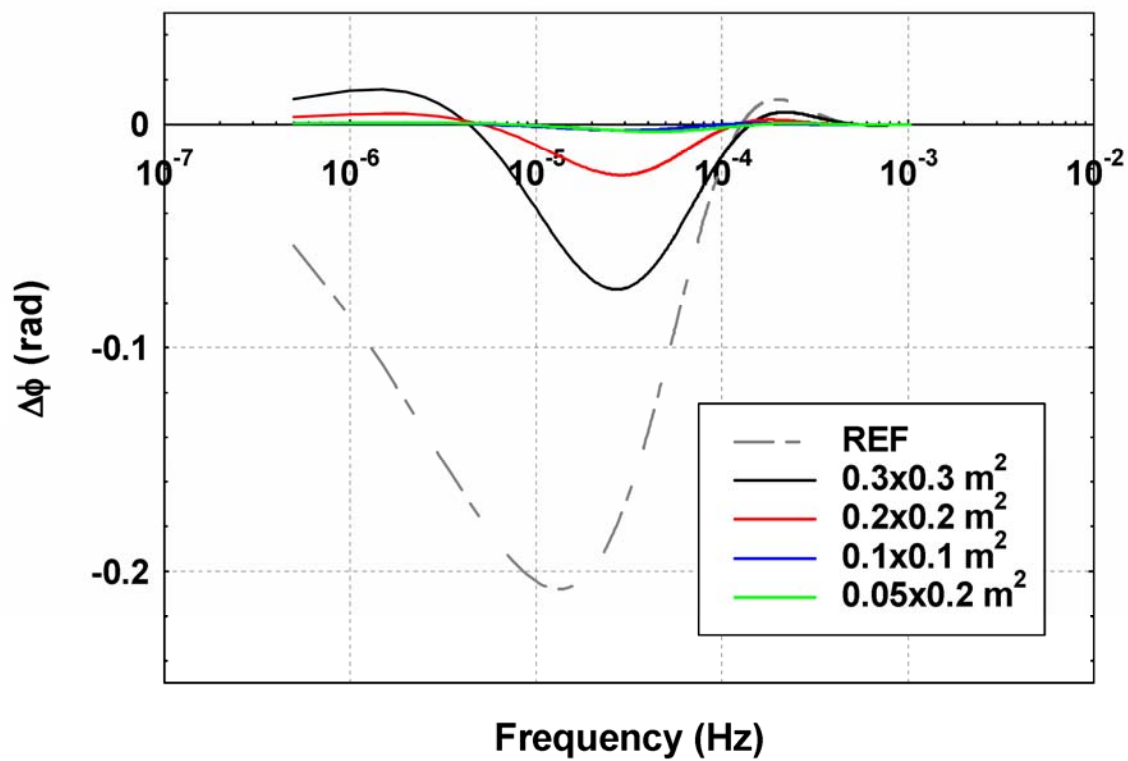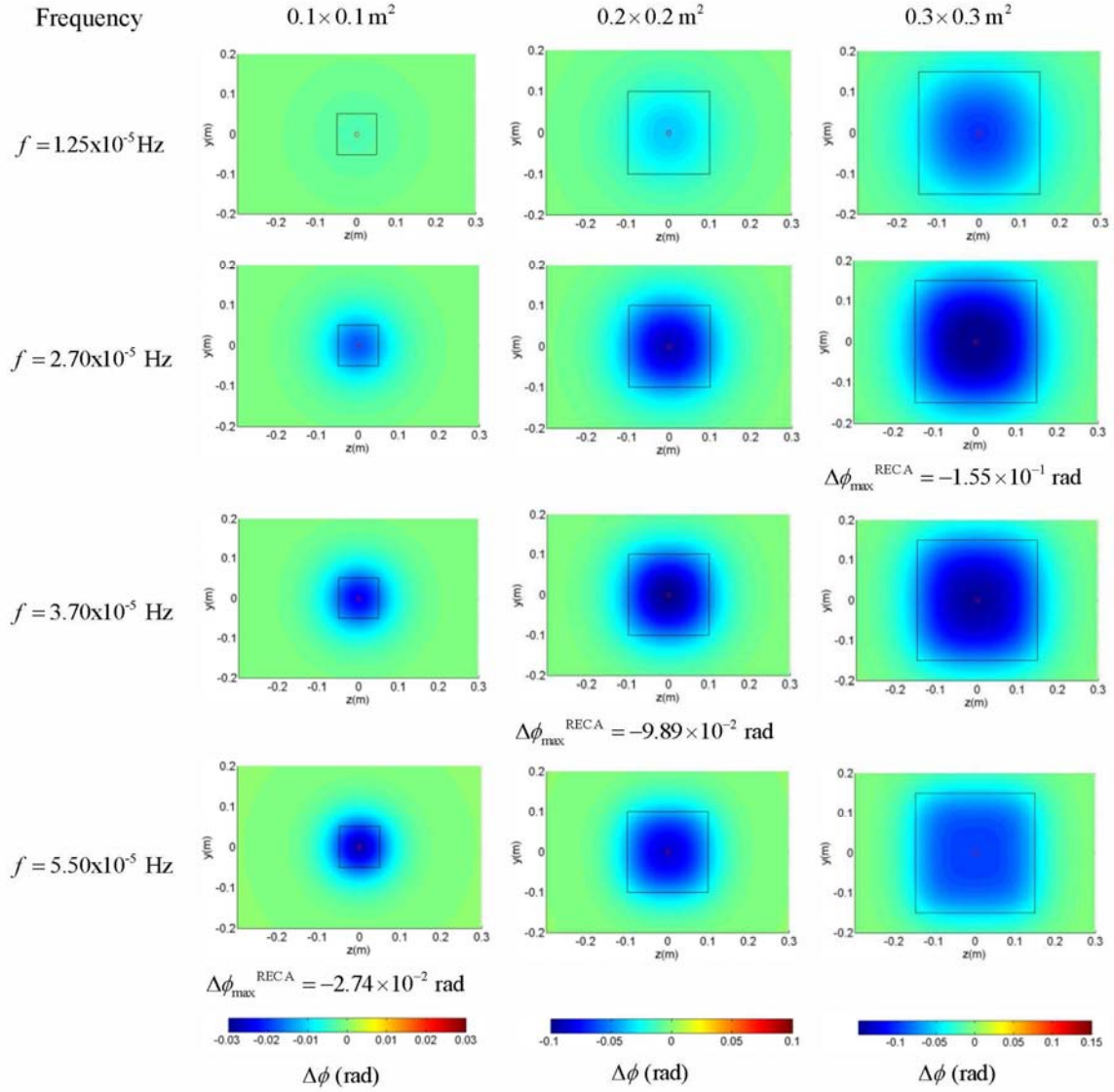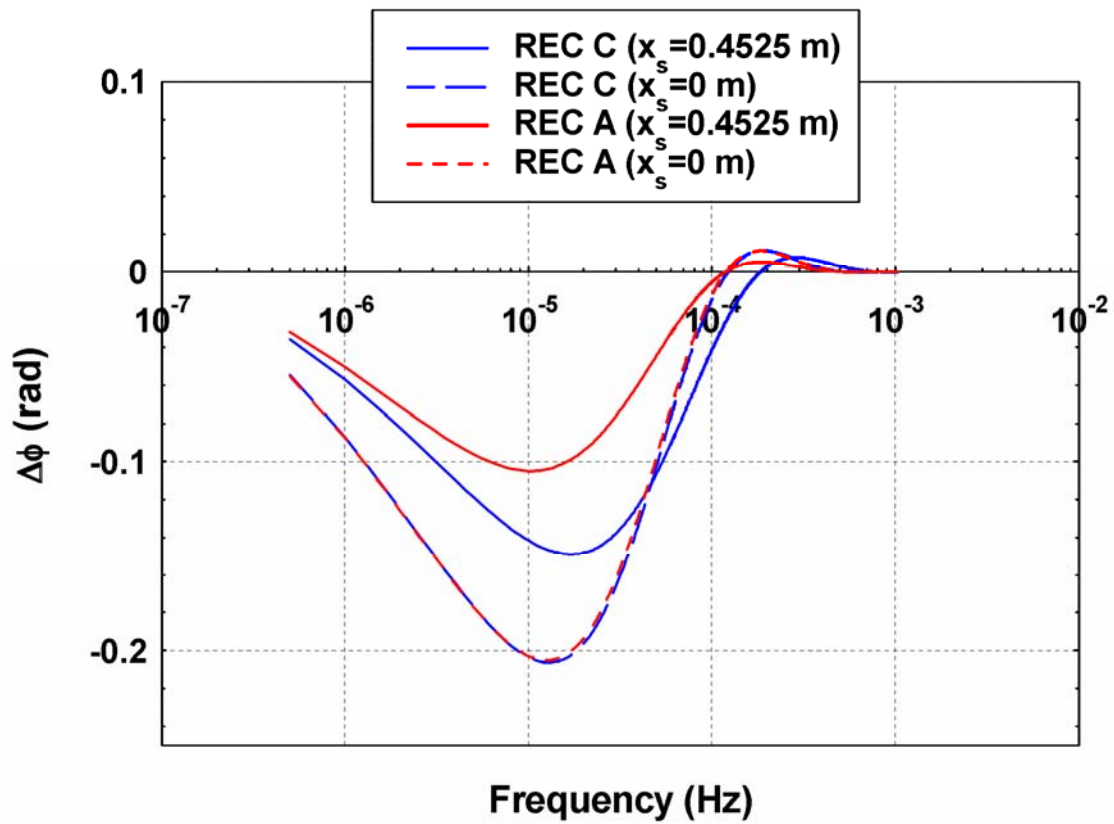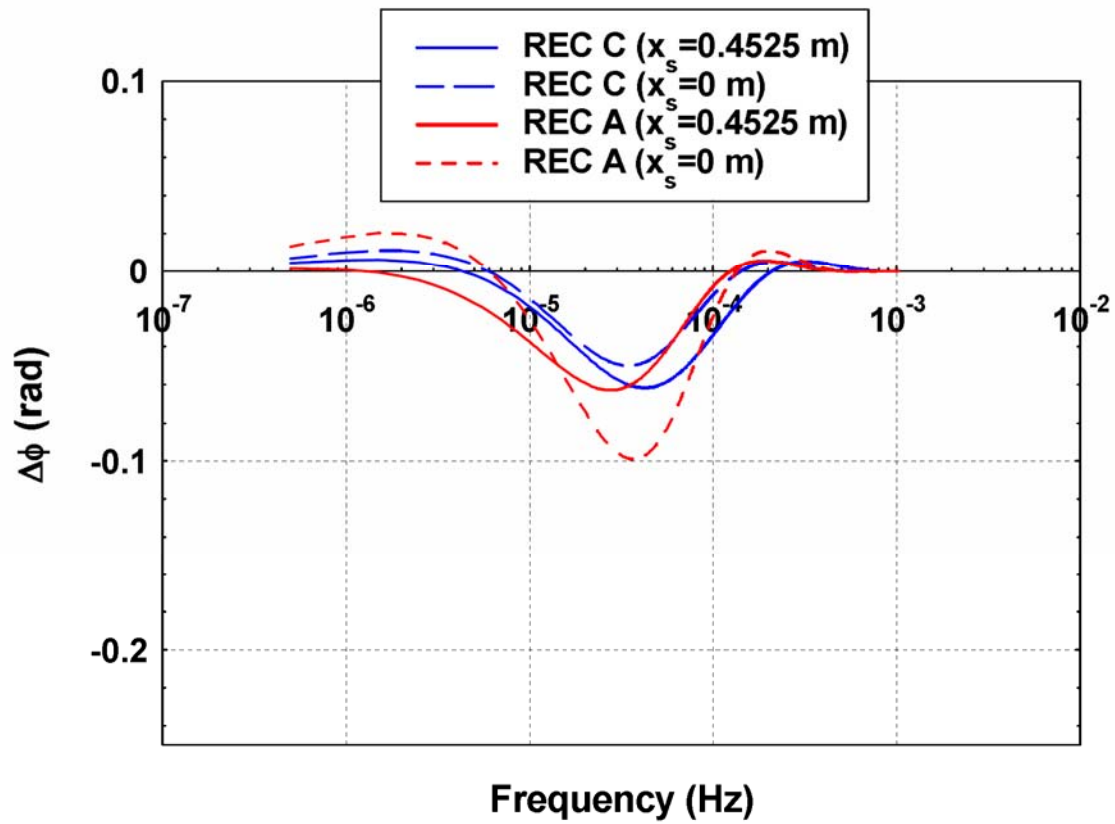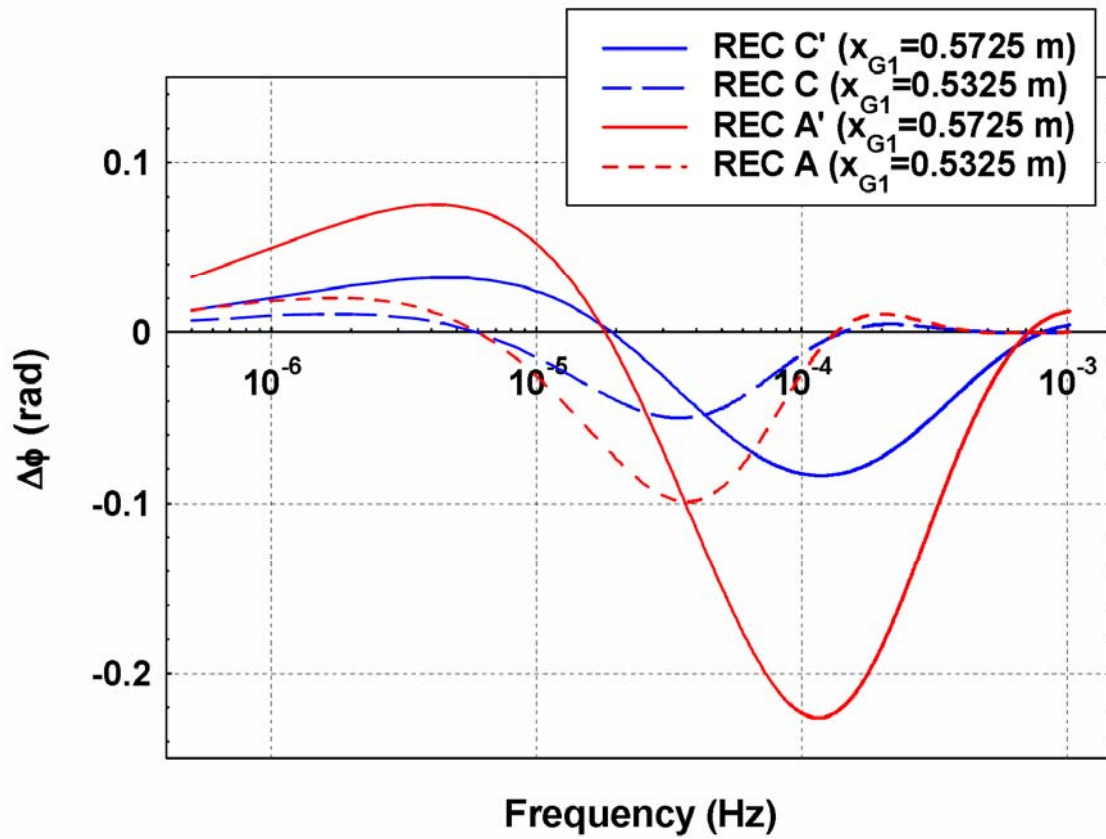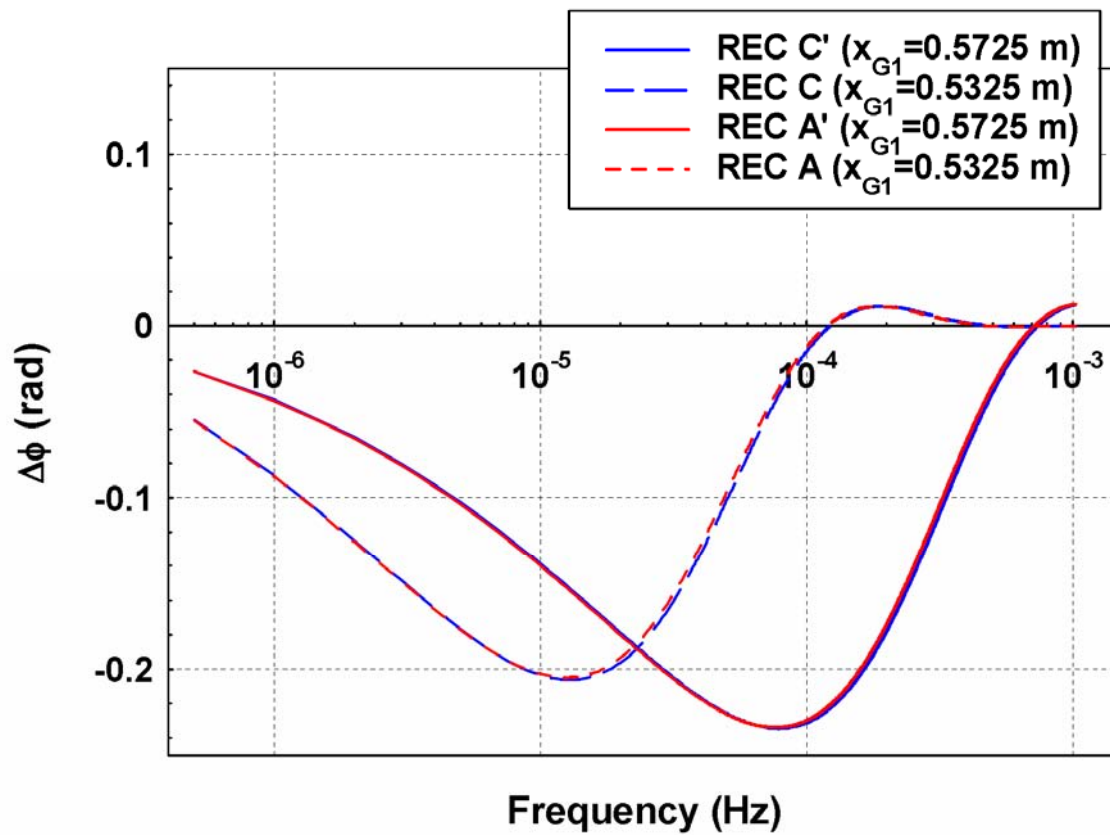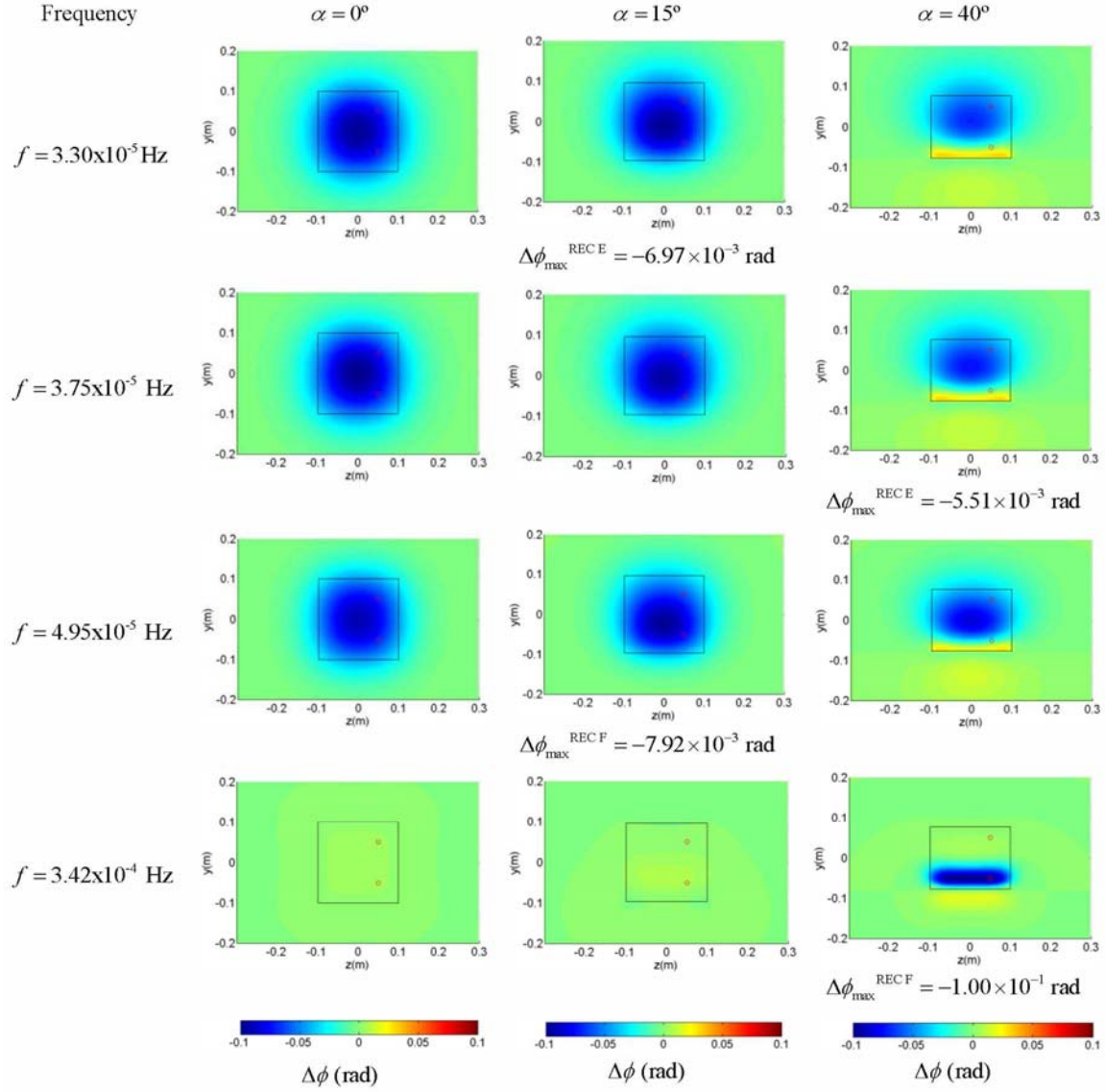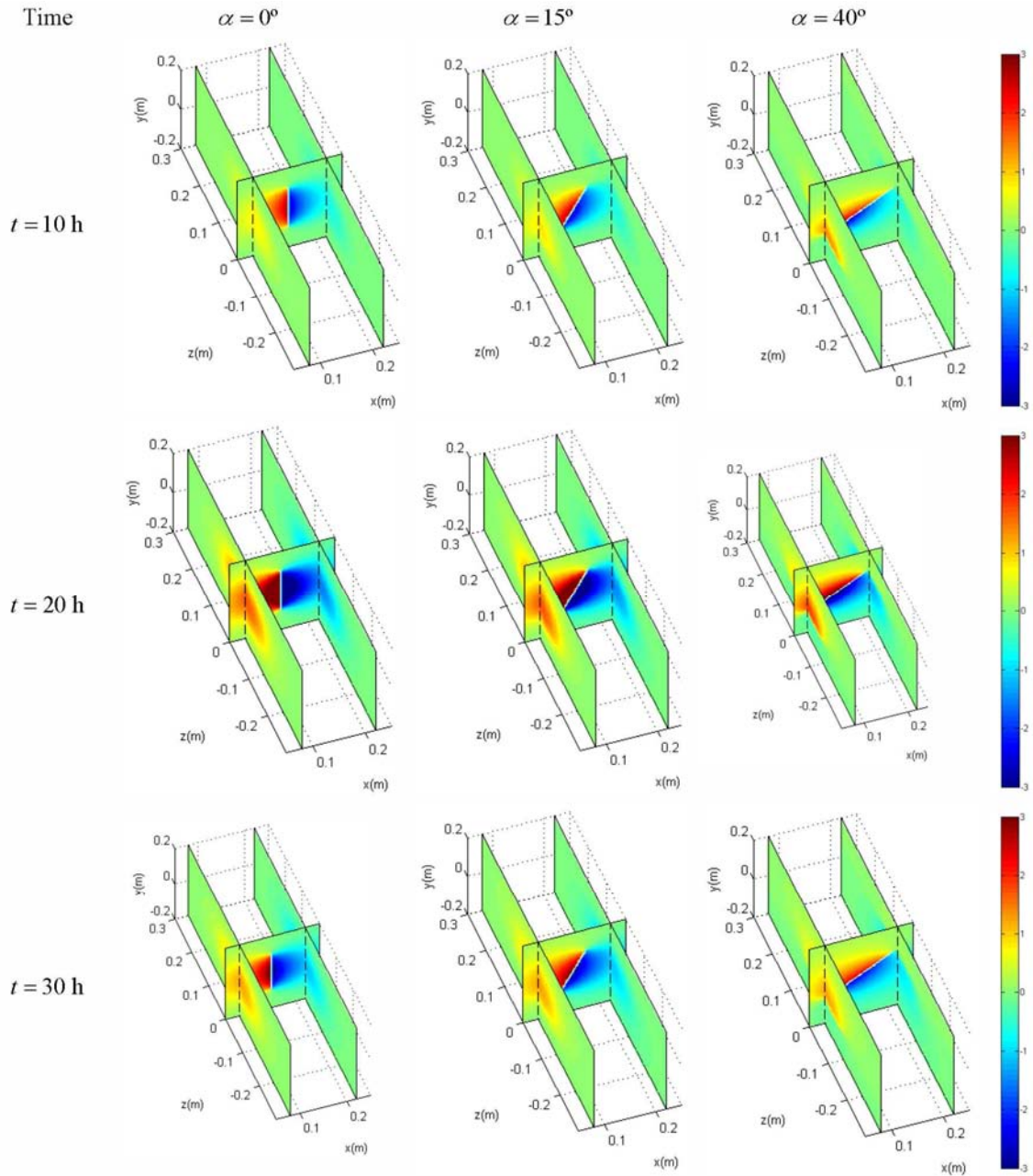
Highlights

- 3D heat diffusion by conduction around a 3D thin crack is modelled;

- A boundary element method in the frequency domain is used to simulate heat diffusion;

- Boundary element is formulated in terms of normal-derivative integral equations (TBEM);

- Phase-contrast images for defect detection using infrared thermography are computed;

- Crack size, shape, position (depth, inclination) and distance to source is studied.